# Chromatic Aberration Correction Using Cross-Channel Prior in Shearlet Domain

Kunyi Li[1][0000−0001−5089−2543] and Xin Jin[1][0000−0001−6655−3888]

Shenzhen International Graduate School, Tsinghua University, Shenzhen, China
li-ky19@mails.tsinghua.edu.cn, jin.xin@sz.tsinghua.edu.cn

**Abstract.** Instead of more expensive and complex optics, recent years, many researches are focused on high-quality photography using lightweight cameras, such as single-ball lens, with computational image processing. Traditional methods for image enhancement do not comprehensively address the blurring artifacts caused by strong chromatic aberrations in images produced by a simple optical system. In this paper, we propose a new method to correct both lateral and axial chromatic aberrations based on their different characteristics. To eliminate lateral chromatic aberration, cross-channel prior in shearlet domain is proposed to align texture information of red and blue channels to green channel. We also propose a new PSF estimation method to better correct axial chromatic aberration using wave propagation model, where F-number of the optical system is needed. Simulation results demonstrate our method can provide aberration-free images while there are still some artifacts in the results of the state-of-art methods. PSNRs of simulation results increase at least 2 dB and SSIM is on average 6.29% to 41.26% better than other methods. Real-captured image results prove that the proposed prior can effectively remove lateral chromatic aberration while the proposed PSF model can further correct the axial chromatic aberration.

## 1 Introduction

Modern camera lenses use a dozen of individual lens elements to minimize optical aberrations but it raises the cost and weight of cameras. Recent years, many researchers turn to much simpler optics such as single-chip lens [1], simple Fresnel lens [2] or the single-ball lens. However, there are still barriers to generate high-quality images with this kind of lightweight equipment. Chromatic aberration (CA) is one of the most severe problems. Because camera lenses have wavelength-dependent refractive indices, it is troublesome to make all color components converge to the same point [3, 4]. This phenomenon often reflects at the edge areas of images. Usually, chromatic aberration can be divided into two categories: axial chromatic aberration (ACA) and lateral chromatic aberration (LCA). The former one may cause the effect of image blurring, which can be corrected by deconvolution, and the later one may cause geometric errors, which can be corrected by image processing [3].

Traditional CA correction methods only focus on one chromatic aberration. Among those LCA correction methods, employing global warping is the most popular one [5]. These global warping methods need a pre-calibration process to estimate parameters. Noticing that CA mainly occurs near the edges, Kim B.K. et al. [6] proposed a method to detect and correct purple fringes using color information with large gradient magnitudes. Pixels in the detected purple fringing regions are desaturated to correct aberration. However, it only works for purple fringes but fails at other color fringes like green fringes. Kang H. et al. [7] developed a partial differential equation based on the study that the edges in the green channel are sharper than those in the red and blue channels. It matches the edges in the red and blue channels to green channel locally. Pi et al. [8] used a spatially variant model to match the gradient and intensity between the red or blue channels and the green channel at the edges. All these methods work well on LCA eliminating. However, without using PSF model of lens, the images are not able to correct ACA.

As for ACA correction, most of these methods choose to use PSFs to deconvolve the images. Schuler et al. [9] presented an aberration removal algorithm for a single lens in YUV color space, which results in a better image quality. He C. et al. [10] proposed a deblurring method using shearlet transform. The power of multiscale and multidirectional analysis and the ability of preserving details of images can be used to surpass the limitation of other methods. Instead of using PSFs for deconvolution, Hosseini et al. [11] proposed a method by convolving the blurry images with inversed PSFs to avoid iterative operation.

Heide F. et al. [1] introduced a convex cross-channel prior using normalized gradient information to correct both ACA and LCA. But it fails to work well on images with complex texture and severe aberrations, since it only uses vertical and horizontal gradient information.

As mentioned above, deconvolution methods with LCA correction priors can correct both two types of aberrations simultaneously, but they need the PSFs of lens. Thus, a proper PSF estimation is needed to acquire better image quality. PSF models are usually proposed by analyzing the statistic of different types of blurry and sharp images. In some circumstances, blur kernels are of parametric forms and these parameters can be estimated from blurry images including spectral methods [12] and edge-based methods [13]. Gokstorp et al. [14] employed the Gaussian function to approximate the blur kernel using a pair of sharp and defocused images. However, in common cases only blurry images are available. Oliveira et al. [15] presented an algorithm using the circular Radon transform. But it would fail for certain scenes because the frequency magnitudes are highly anisotropic. A General Gaussian model was proposed using edge detection and re-blur approach by Liu et al. [16]. It established a LUT between PSFs and parameters for further use. However, all of these methods were based on statistic models and ignored wave propagation characters.

In this paper, based on the distribution of color and texture information of images in RGB channels, we propose a robust aberration correction approach which corrects both LCA and ACA. Cross-channel prior in shearlet domain (CC-SD prior) is introduced to align red and blue channels to green channel, the sharpest channel. Clear images are recovered and LCA is effectively suppressed.

PSNR and SSIM have significant improvements in simulation results. Moreover, to deal with ACA in real-captured images, a more precise PSF estimation method based on wave propagation model is presented. Results demonstrate that CC-SD prior combined with wave propagation PSF model can remove LCA and ACA efficiently.

The rest of this paper is organized as follows. Section 2 presents analysis of color and texture information distribution and the CC-SD prior. Section 3 shows proposed PSF estimation model. Section 4 shows experimental results including simulations and real-captured images. Conclusion is drawn in Section 5.

## 2 Cross-Channel Prior in Shearlet Domain

In this section, we propose a new prior to deal with LCA, which takes edges from all direction into account and can handle much severer aberration. We start by demonstrating image restoration model and introducing the novel CC-SD prior to correct LCA. Then Alternating Direction Method of Multipliers (ADMM) is used to solve the minimization problem.

### 2.1 LCA Correction Model Using CC-SD Prior

Reconstructing the original image from blurry image can be carried out within the framework of image deconvolution. However, it is a well-known highly ill-posed problem because only blurry image is known. Regularization terms were introduced to constraint this problem. In general, many regularization methods lead to the following minimization function:

$$\min_x \|Hx - y\|_2^2 + \frac{\beta_1}{2}\,\mathrm{S}(x) + \frac{\beta_2}{2}\,\mathrm{J}(x), \tag{1}$$

where $x$ denotes the recovered clear image. $y$ is observed blurry image. The first term is called data fidelity term. $H$ is the convolution operator related to spatially invariant PSF in matrix form. The second and third terms are regularization terms. $\mathrm{S}(x)$ enforces a heavy-tailed distributed for gradients, like total-variation [17] or shearlet-regularization [10]. $\mathrm{J}(x)$ implements a special constraint to correct LCA. $\beta_1, \beta_2$ are penalty factors which keep the compromise between the data fidelity term and the regularization terms.

The main idea of our proposed method is to align the image texture, like fringes, of red and blue channels to green channel. For red or blue channel, the regularization term $\mathrm{J}(x)$ is defined as:

$$\mathrm{J}(x) = \|\,\mathrm{T}(x_G) - \mathrm{T}(x)\|_2^2, \tag{2}$$

where $x$ is latent red or blule channel image. $\mathrm{T}(x)$ represents the texture information extracted from the red or blue channel. $x_G$ is the green channel image recovered by an existing method, such as PSA method [10]. $\mathrm{T}(x_G)$ represents the texture information extracted from green channel.

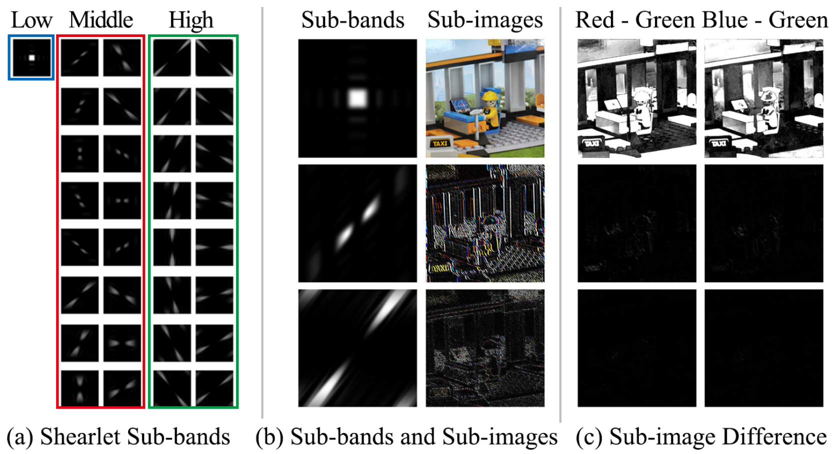


**Fig. 1.** (a) Shearlet sub-bands in frequency domain. Images in blue, red and green rectangles are low-frequency, middle-frequency and high-frequency sub-bands, respectively. (b) Three sub-bands and their corresponding sub-images. First, second and last rows are images of one low-frequency, one middle-frequency and one high-frequency sub-bands and their corresponding sub-images, respectively. (c) Difference of sub-images between red/blue and green channel. The whiter the figures are, the larger difference is between two sub-images.

To extract texture information from images, instead of gradients which only use vertical and horizontal edge information, we apply shearlet transform [18–20] which is a multiscale and multidirectional analysis method. Shearlet transform of $x$ can be implemented in frequency domain by component-wise multiplication:

$$\mathrm{SH}_j(x) = \mathfrak{F}^{-1}(\hat{H}_j . * X), \tag{3}$$

where $X$ denotes the Fourier transform of $x$ and $\hat{H}_j$ is the frequency domain shearlet base of the $j^{th}$ sub-band. $.*$ denotes the component-wise multiplication operator. $\mathfrak{F}^{-1}(.)$ is the inverse Fourier transform operator. Shearlet transform decomposes the images into several sub-images in frequency domain, including one low frequency component and numbers of middle and high frequency components. The number of sub-bands depends on the shearlet level. Therefore, $\mathrm{T}(x)$ can be written as:

$$\mathrm{T}_i(x) = \mathfrak{F}^{-1}(\hat{H}_i . * X), \tag{4}$$

where $\hat{H}_i$ is the middle and high frequency sub-bands, $\mathrm{T}_i(x)$ represents the corresponding sub-image of $i^{th}$ sub-band. Fig. 1 shows the result of shearlet transform on an aberration-free image. Fig. 1(a) demonstrates the sub-bands of a level 3 shearlet transform. These are filters of different frequency ranges and directions in frequency domain. Fig. 1(b) shows three sub-bands and its corresponding sub-images. Low frequency sub-image contains most information of the image, including color information. Middle and high frequency sub-images are texture information of a selected direction. Fig. 1(c) proves our assumption that color information only exists in low-frequency components and texture information of three channels are approximately the same.

With the above notations, the proposed optimization problem for red and blue channel is:

$$\min \|Hx - y\|_2^2 + \frac{\beta_1}{2}\sum_j \| \mathrm{SH}_j(x)\|_1 + \frac{\beta_2}{2}\sum_i \| \mathrm{T}_i(x_G) - \mathrm{T}_i(x)\|_2^2, \tag{5}$$

where the second term is the shearlet-regularization term [10] used to suppress the ring effect. The third term is proposed CC-SD prior. $\beta_1, \beta_2$ are penalty factors.

### 2.2 Optimization Using ADMM

In this subsection, we use ADMM [21] to solve the optimization problem. To solve the $L_1$–norm simply, we introduce auxiliary variables $f_i$ for each $L_1$-norm term. To avoid the inner iterations, another auxiliary variable $u$ is employed for $Hx$. The corresponding augmented Lagrangian function is defined as:

$$\begin{aligned}\mathcal{L}(x,u,f;\mu,\xi,\gamma) \triangleq & \frac{\alpha}{2}\|u - Hx\|_2^2 - < \mu, u - Hx > + \delta_\Omega(u) + \sum_j \|f_j\|_1 \\ & + \frac{\beta_1}{2}\sum_j \|f_j - \mathrm{SH}_j(x)\|_2^2 - \sum_j < \xi_j, f_j - \mathrm{SH}_j(x) > \\ & + \frac{\beta_2}{2}\sum_i \| \mathrm{T}_i(x_G) - \mathrm{T}_i(x)\|_2^2 - \sum_i < \gamma_i, \mathrm{T}_i(x_G) - \mathrm{T}_i(x) >,\end{aligned} \tag{6}$$

where $f_i$ and $u$ are auxiliary variables, and

$$\delta_\Omega(u) = \begin{cases} 0, & \text{if } u \in \Omega \triangleq \{u : \|u - y\|_2^2 \le c\} \\ +\infty, & \text{otherwise} \end{cases},$$

The inequality constraint is related to Morozov's discrepancy principle [22], $c = \tau n^2\sigma^2$. $\sigma^2$ is the white noise variance of image. $\tau = -0.006 * BSNR + 1.09$, $BSNR = \log_{10}(\frac{\|y - mean(y)\|_2^2}{n^2\sigma^2})$, $\mu, \xi_j, \gamma_i$ are Lagrange multipliers, $\alpha, \beta_1, \beta_2 \ge 0$ are penalty parameters. According ADMM, we can solve the following subproblems alternatively:

$$\begin{cases} x^{k+1} = \arg\min_x \frac{\alpha}{2}\|u^k - Hx - \frac{\mu^k}{\alpha_1}\|_2^2 + \frac{\beta_1}{2}\sum_j \|f_j^k - \mathrm{SH}_j(x) - \frac{\xi^k}{\beta_1}\|_2^2 \\ \qquad\qquad + \frac{\beta_2}{2}\sum_i \| \mathrm{T}_i(x_G) - \mathrm{T}_i(u) - \frac{\gamma^k}{\beta_2}\|_2^2 \\ f_j^{k+1} = \arg\min_{f_j} \|f_j\|_1 + \frac{\beta_1}{2}\|f_j - \mathrm{SH}_j(x^{k+1} - \frac{\xi_j^k}{\beta_1})\|_2^2 \\ u^{k+1} = \arg\min_u \delta_\Omega(u) + \frac{\alpha}{2}\|u - Hx^{k+1} - \frac{\mu^k}{\alpha}\|_2^2 \\ \mu^{k+1} = \mu^k - \alpha(u^{k+1} - Hx^{k+1}) \\ \xi_j^{k+1} = \xi^k - \beta_1(f_j^{k+1} - \mathrm{SH}_j(x^{k+1})) \\ \gamma_i^{k+1} = \gamma_i^k - \beta_2(\mathrm{T}_i(x_G) - \mathrm{T}_i(x)) \end{cases} . \tag{7}$$

The minimization subproblem with respect to $x$ has three quadratic terms and can be solved through FFT and IFFT [17]. Subproblem respect to $f_i$ can be expressed in the form of 1D soft-threshold shrinkage. And sub-problem with respect to $u$ can be solved by He's method [10].

## 3 PSF Estimation Based on Wave Propagation

Previous section only focuses on LCA correction. In this section, we deal with ACA by proposing a new PSF estimation model for further deconvolution. The main influence of blurring reflects on edges. Therefore, the blurring degree of edges may determine parameters of PSF, like the shape and size. Here, we define a parameter called gradient ratio:

$$R = \frac{\nabla y}{\nabla y_1} = \frac{\nabla(h * x)}{\nabla(h * x * h_g(\sigma_0))} \tag{8}$$

where $y$ represents edge patches extracted from blurry image. $y_1$ represents a re-blurred edge patch using $y$ convolve with a given Gaussian function. $\nabla$ is the gradient operator. $h$ is unknown PSF of the imaging system. Fig. 2(a) and Fig. 2(b) illustrate the flow chart of the algorithm. First, edge detection is used. Fig. 2(c) shows four templates for edge detection. Then, gradient ratio distribution $R_0$ of the blurry and re-blurred edges is computed [16] by $R_0 = \frac{\nabla y(0,0)}{\nabla y_1(0,0)}$. The remaining problem is to link $R_0$ with parameters of the unknown PSF $h$.

In the sub-sections, instead of only use the statistic model, wave propagation model is used to establish a LUT between $R_0$ and aberration parameters. Then, the computed $R_0$ can determine a unique PSF.

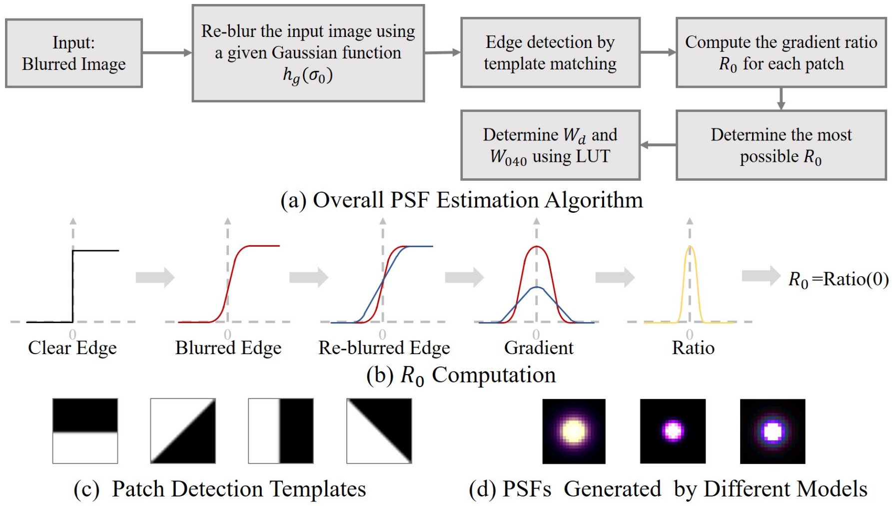


**Fig. 2.** (a) Flow chart of PSF estimation algorithm. (b) Flow chart of $R_0$ computation. (c) 4 templates for patch detection. (d) First column is a PSF generated by Gaussian model [22] where $\sigma_0 = (4, 2, 7)$. Second column is a PSF generated by General Gaussian model [15] where $\beta_0 = (1.9, 1.2, 2.2)$. Third column is a PSF generated by proposed model where $W_d = (-1, 0.5, 2)$ and $W_{040} = (0.4, 0.1, 0.5)$.

### 3.1 Wave Propagation Model

For any image system, aberrated pupil function is described as [23]:

$$\mathrm{P}(W_d, W_{040}; u, v) = \mathrm{circ}(\frac{\sqrt{u^2+v^2}}{w_{XP}}) \exp(-j\frac{2\pi}{\lambda}\mathrm{Se}(W_d, W_{040}; \frac{u}{w_{XP}}, \frac{u}{w_{XP}})), \quad (9)$$

where $\mathrm{Se}(W_d, W_{040}; \frac{u}{w_{XP}}, \frac{v}{w_{XP}}) = W_d((\frac{u}{w_{XP}})^2 + (\frac{v}{w_{XP}})^2) + W_{040}((\frac{u}{w_{XP}})^2 + (\frac{v}{w_{XP}})^2)^2$ is Seidel Polynomials, which is used to describe aberrations for optical systems. $W_d$ defines defocus aberration and $W_{040}$ defines spherical aberration. $u, v$ are physical coordinates of exit pupil. $w_{XP}$ is the diameter of exit pupil. $\lambda$ represents wavelength. And $\mathrm{circ}(X)$ is a circular function where $\mathrm{circ}(X) = 1$ if $X \leq 0.5$ and $\mathrm{circ}(X) = 0$ if $X > 0.5$. According to the computational Fourier optics [23], PSF of this image system can be written as

$$\mathrm{h}_{WP}(W_d, W_{040}; u, v) = |\mathfrak{F}^{-1}\{\mathrm{P}(W_d, W_{040}; -2\lambda w_{XP} f^{\#} f_U, -2\lambda w_{XP} f^{\#} f_V)\}|^2, \quad (10)$$

where $\mathfrak{F}^{-1}$ is inverse Fourier transform operator. $f^{\#}$ is F-number of the optical system, $f_U, f_V$ is frequency of the senor plane, $\lambda$ is wavelength. Fig. 2(d) shows PSFs generated by different estimating models.

### 3.2 Establish the LUT Between $W_d, W_{040}$ and $R_0$

PSF is assumed as spatially invariant. According to the gradient-based framework [24], the relationship between $W_d, W_{040}$ and $R_0$ can be written as:

$$R_0 = \frac{\nabla y(0,0)}{\nabla y_1(0,0)} = \frac{\int_{-\infty}^{\infty} \mathrm{h}_{WP}(W_d, W_{040}, 0, v)\, dv}{\int_{-\infty}^{\infty} \mathrm{h}(W_d, W_{040}, \sigma_0, 0, v)\, dv} \tag{11}$$

where $\mathrm{h}_{WP}(W_d, W_{040}, 0, v)$ denotes the magnitudes along the y-axis of blur kernel, and $\mathrm{h}(W_d, W_{040}, \sigma_0, 0, v) = \iint_{-\infty}^{\infty} \mathrm{h}_{WP}(W_d, W_{040}, u-\xi, v-\eta)\, \mathrm{h}_g(\sigma_0, \xi, \eta)\, d\xi\, d\eta$. However, it is difficult to have an analytical solution among $W_d$, $W_{040}$ and $R_0$, A LUT is pre-established by varying $W_d$ and $W_{040}$, and corresponding $R_0$ can be calculated by Eq.(11). Using this LUT, Seidel parameters can be located by computing $R_0$ from blurry images. Then the PSF $h$ can be reconstructed.

## 4 Experiments

In this section, we present experimental results including simulation results and real-captured images provided by our lens system which have severe optical aberrations. We apply the proposed method and make a comparison with other state-of-art methods. Codes of comparison methods are downloaded from GitHub provided by the authors.

### 4.1 Experiment Image Sets and Parameters Setting

**Table 1.** Computational Time (Seconds).

| | IGM[8] | CC[1] | PSA[10] | IDBP[25] | TRI[26] | 1Shot[11] | **Proposed** |
|---|---|---|---|---|---|---|---|
| Buildings | 683 | 1668 | 674 | 787 | / | / | **860** |
| Cars | 689 | 1968 | 680 | 779 | / | / | **854** |
| LEGO | 687 | 1758 | 674 | 773 | / | / | **857** |
| Windows | 689 | 1974 | 680 | 763 | / | / | **858** |
| LEGO | 685 | 1570 | 677 | 1057 | 454 | 0.58 | **862** |
| Taxi | 692 | 1281 | 678 | 917 | 521 | 0.45 | **865** |
| Workers | 696 | 1944 | 676 | 946 | 456 | 0.25 | **866** |

Four simulation images and three captured images are tested. The size of each image is $720 * 720$. These images are suitable for illustrating the potential of proposed algorithm, because they possess abundant details.

Simulation images are captured by Sony ILCE 7 Mark 3 with Tamron 28-75mm lens, one of the best commercial cameras, which can be regarded as aberration-free images. Images include one indoor scene, image LEGO, and three

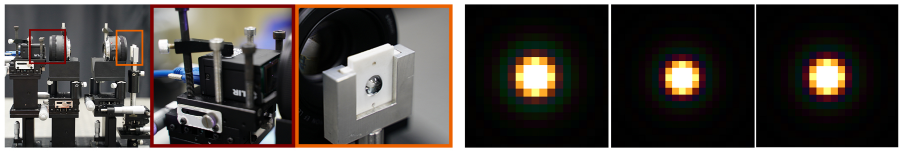

(a) Single-ball lens system (b) Estimated PSFs

**Fig. 3.** (a) Single-ball lens with a 4F system. The ball lens and sensor are shown in orange and red rectangles, respectively. (b) Estimated PSFs of single-ball lens system.

outdoor scenes. Image Buildings and image Cars have rich texture details. Image Windows shows a significant color bias. To get blurry images, we convolved each image in three channels with different blur kernel, as shown in Fig. 2(d).

Real-captured images are acquired from our sing-ball lens system, as shown in Fig. 3(a). Image Taxi shows a blue toy car while the wheel appears significant purple fringe. Image Workers suffers less chromatic aberration but still there is a green fringe on the face of the toy worker. Image LEGO is much vaguer which makes it more difficult to estimate PSF.

To balance the convergence speed and result performance, we set $\alpha = 10 * \beta_1, \beta_1 = \beta_2 = 1$ in the simulation process and $\alpha = 0.1 * \beta_1, \beta_1 = \beta_2 = 1$ in real-captured images process. For shearlet transform, ShearLab 3D toolbox is used and a shearlet level 3 is set. During PSF estimation process, we set $f^{\#} = 1.2$. $W_d$ and $W_{040}$ vary from -3 to 3 and 0.1 to 2 with an interval of 0.05, respectively, while we establish LUT. Experiments are tested on a PC with Intel® Core™ i7-9700 CPU 3.00GHz and 8GB RAM. Time consumption is shown in Table 1

### 4.2 Comparison of Simulation Results

In this sub-section, we compared the proposed CC-SD prior with other 4 state-of-art methods, including methods which only use convex optimization, methods which only process deblurring, and methods which correct color fringes while deblurring. Pi et al. [8] presented a convex optimization method using intensity and gradient matchings (IGM). But it only corrects LCA. Heide F. et al. tried to align three channels by a Cross-Channel prior [1] while deblurring. The results of PSA method [10] demonstrate that our CC-SD prior indeed corrects the color misalign. IDBP [25] solves the inverse problems using off-the-shelf denoisers, which requires less parameter tuning. All algorithms in this sub-section were fed with the same PSFs for deconvolution, and ran until the per-iteration change fell below a given threshold. As for the evaluation criterion, PSNR and SSIM are shown in this section and visual performance is also considered. As for visual performance evaluation, we mainly focus on the sharpness and color consistency of edges.

Fig. 4-7 demonstrate 4 different results. In each figure, sub-figure (a) is the original image, and sub-figure (b) is the blurry image. Three selected areas are magnified and fringes can be seen distinctly. Sub-figures (c) to (f) are recovered

**Table 2.** PSNR (dB)/SSIM Comparison of Simulation result.

| | Blurry | IGM[8] | CC[1] | PSA[10] | IDBP[25] | **Proposed** |
|---|---|---|---|---|---|---|
| Buildings | 18.40/0.54 | 20.58/0.63 | 18.88/0.80 | 20.76/0.81 | 20.40/0.78 | **24.64/0.89** |
| Cars | 19.70/0.63 | 21.58/0.71 | 19.98/0.81 | 22.37/0.84 | 22.01/0.83 | **25.11/0.90** |
| LEGO | 24.46/0.88 | 26.48/0.92 | 24.25/0.88 | 29.28/0.96 | 28.48/0.95 | **31.90/0.98** |
| Windows | 19.09/0.66 | 20.81/0.73 | 19.39/0.82 | 21.44/0.95 | 21.08/0.85 | **24.71/0.91** |

images using the state-of-art algorithms and sub-figure (g) is recovered image using our CC-SD prior.

Fig. 4 shows a number of buildings. The result of IGM method shows the least color fringes, however it causes desaturation and image is still blurry. Since these details are small but rich, Cross-Channel method only recovers a sharper image but the color fringes are still existed. Our proposed algorithm presents a sharp image with almost none color fringe. Fig. 5 shows a business street. There is a significant degradation on advertising boards after blurring. Among these recovery algorithms, our result is the most approximate one to the original image. In Fig. 6, our algorithm shows a better performance in sharpness and color consistency as well. Fig. 7 displays a yellow wall with a white window, in which exists a distinct color bias. Due to advantage of CC-SD prior, color bias cannot interfere the performance of our algorithm. However, result of Cross-Channel Prior shows an obvious color shift. PSA and IDBP methods provide acceptable results but still with some purple fringes.

PSNR and SSIM of all methods is demonstrated in Table 2. Note that our algorithm consistently outperforms than others. Overall, the proposed method is able to reconstruct the textures and show more clear and clean edges than other approaches.

### 4.3 Comparison of Real-Captured Image Results

In this sub-section, all algorithms contain two steps, PSFs estimation and image deconvolution, except for IGM method. Proposed algorithm is compared with other 6 state-of-art methods. Cross-Channel Prior [1], PSA [10] and IDBP [25] were fed with the same PSFs estimated by proposed wave-propagation method. TRI [26] method uses the three segments of intensity prior which is motivated by that the blur process destroys the sparsity of intensity, and shrinks the distance between two distinct gray levels. 1ShotMaxPol [11] calculates the inversed PSF and convolves with images to avoid iterative process. The results of proposed prior without ACA correctionis are also present to show the effect of LCA and ACA correction, respectively.

For real-captured images, we only compared the visual performance of each methods. Fig. 8-10 demonstrate the captured blurry images and results using different methods. The corresponding estimated PSFs are shown in Fig 3(b). Three

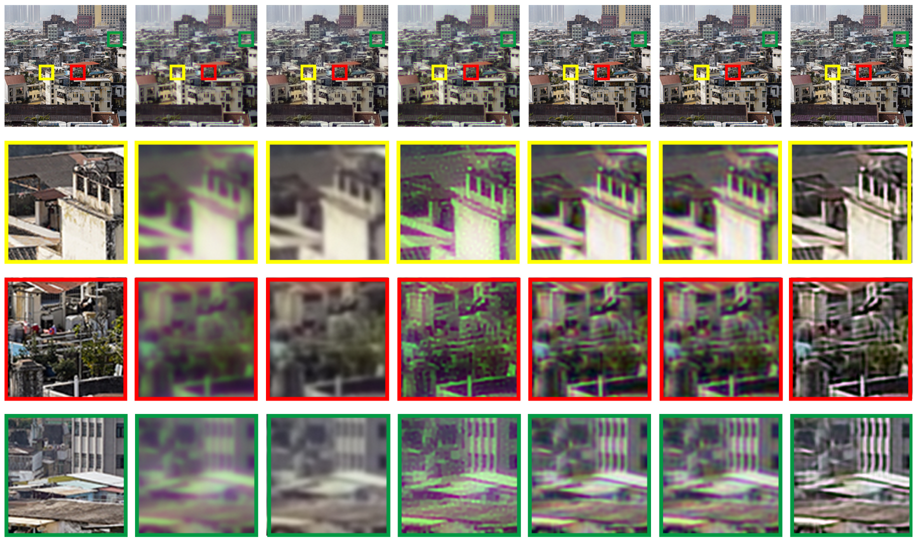

(a) Original (b) Blurred (c) IGM [8] (d) Cross Channel [1] (e) PSA [10] (f) IDBP [25] (g) Proposed

**Fig. 4.** Buildings. Full images and three selected areas marked by yellow, red and green rectangles respectively.


(a) Original (b) Blurred (c) IGM [8] (d) Cross Channel [1] (e) PSA [10] (f) IDBP [25] (g) Proposed

**Fig. 5.** Cars. Full images and three selected areas marked by yellow, red and green rectangles respectively.

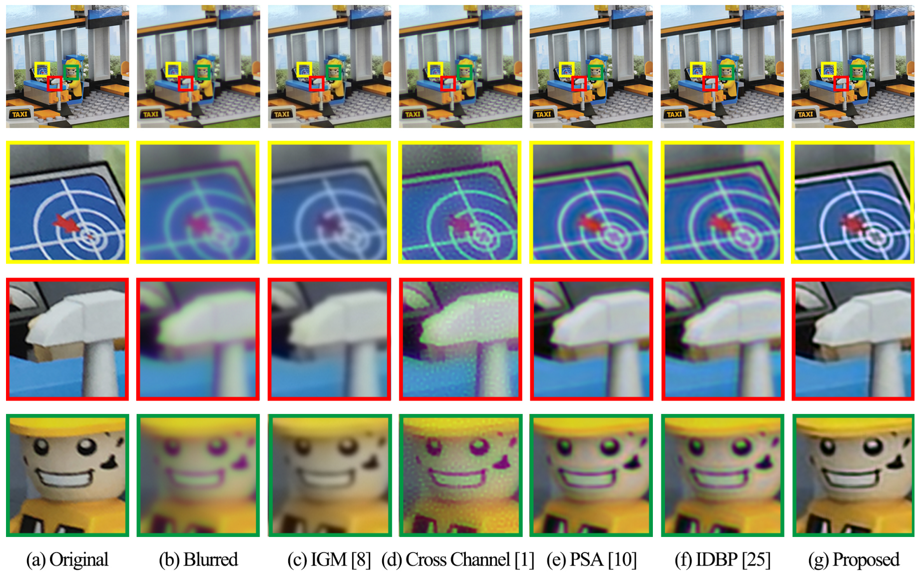

Fig. 6. LEGO. Full images and three selected areas marked by yellow, red and green rectangles respectively.

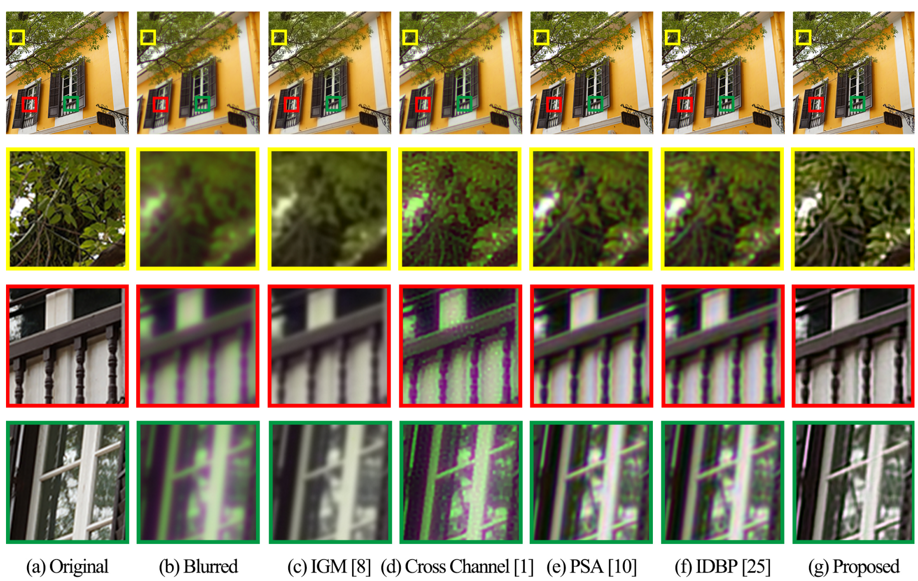

Fig. 7. Windows. Full images and three selected areas marked by yellow, red and green rectangles respectively.

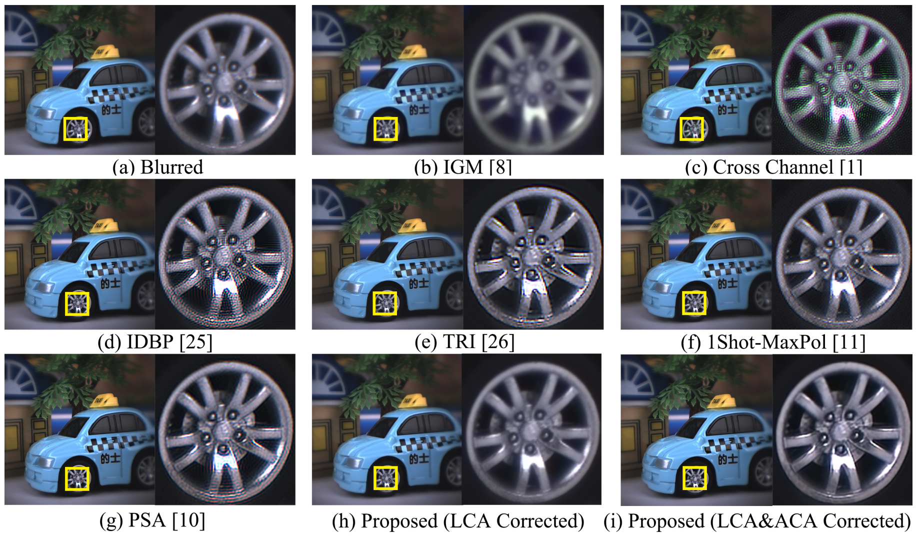


**Fig. 8.** Taxi. (a)-(i) Full images and a selected area marked by yellow rectangle.

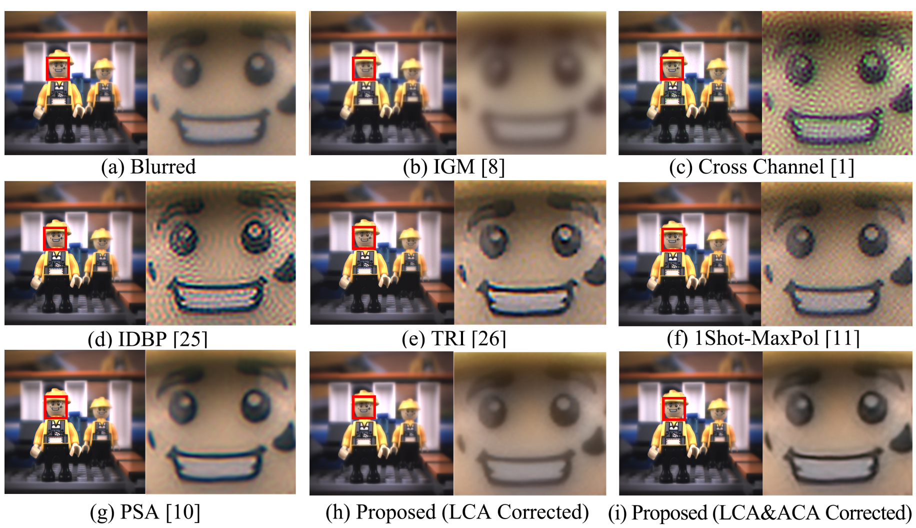


**Fig. 9.** Workers. (a)-(i) Full images and a selected area marked by yellow rectangle.

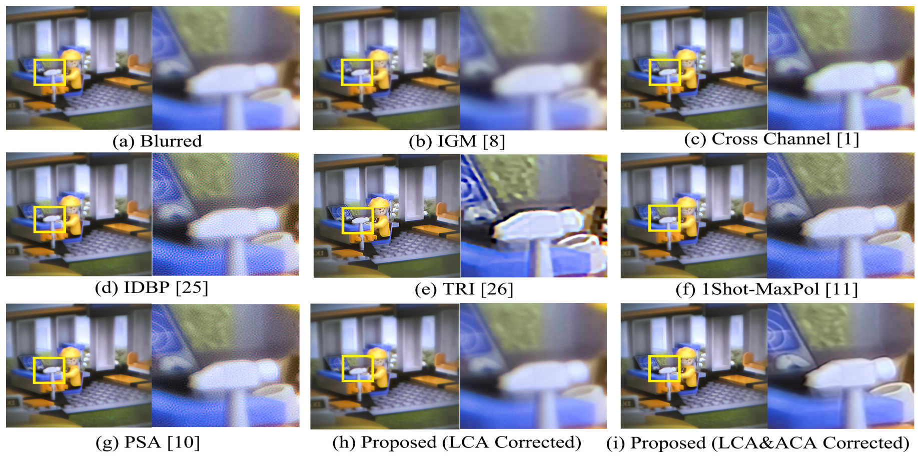


**Fig. 10.** LEGO. (a)-(i) Full images and a selected area marked by yellow rectangle.

different scenes were tested and a square area has been magnified to demonstrate details of results. Although some approaches may have more clear edges, it may increase some artifacts as cost, such as ring effect and distinct noise. IGM method eliminates the color fringes effectively. The wheel of captured image has severe purple fringes. Fig. 8(b) shows a totally chromatic-aberration-free but it is still blurry. Fig. 8 and Fig. 9 have a certain degree of color deviation and affect the results of Cross-Channel method significantly. All results of TRI method have a sense of smear in images, as Fig. 10(e) shows. 1Shot-MaxPol method provides good quality of images but raises some regular unnatural texture and color fringes still can be seen. Results of PSA method show sharp images but contain color fringes. Results of LCA correction only, like Fig. 9(h), show chromatic-aberration-free images but they remain blurry. The proposed method produces both sharp images and correct images.

## 5 Conclusion

In the current study, a novel LCA correction method was conducted by introducing the cross-channel prior in shearlet domain. Employing the CC-SD prior while deconvolving, we corrected both LCA and ACA. Details can be preserved and image quality can be promoted by our method. Wave-propagation model for PSFs estimation was proposed to help deal with ACA in real-captured images. This model takes Seidel Polynomials into account and surpasses the limitation of statistic models. Experiments indicated that the proposed algorithm is competitive in PSNR, SSIM and visual performance.

**Acknowledgment.** The work was supported in part by National Natural Science Foundation of China (Grant No. 61827804 and 61991450).

## References


1. Heide, F., Rouf, M., Hullin, M.B., Labitzke, B., Kolb, A.J.A.T.o.G.: High-quality computational imaging through simple lenses. **32** (2013) 149:1–149:14
2. Nikonorov, A., Petrov, M., Bibikov, S., Yuzifovich, Y., Yakimov, P., Kazanskiy, N., Skidanov, R., Fursov, V.: Comparative evaluation of deblurring techniques for fresnel lens computational imaging. In: 2016 23rd International Conference on Pattern Recognition (ICPR). (2016) 775–780
3. Thibos, L.N., Bradley, A., Still, D.L., Zhang, X., Howarth, P.A.J.V.R.: Theory and measurement of ocular chromatic aberration. **30** (1990) 33–49
4. Marimont, D.H., Wandell, B.A.: Matching color images: the effects of axial chromatic aberration. J. Opt. Soc. Am. A **11** (1994) 3113–3122
5. Boult, T.E., Wolberg, G.: Correcting chromatic aberrations using image warping. In: CVPR. (1992) 684–687
6. Kim, B.K., Park, R.H.: Automatic detection and correction of purple fringing using the gradient information and desaturation. In: 2008 16th European Signal Processing Conference, IEEE (2008) 1–5
7. Kang, H., Lee, S.H., Chang, J., Kang, M.G.: Partial differential equation-based approach for removal of chromatic aberration with local characteristics. Journal of Electronic Imaging **19** (2010) 033016
8. Pi, L., Wang, W., Ng, M.: A spatially variant total variational model for chromatic aberration correction. Journal of Visual Communication and Image Representation **41** (2016) 296–304
9. Schuler, C.J., Hirsch, M., Harmeling, S., Schölkopf, B.: Non-stationary correction of optical aberrations. In: 2011 International Conference on Computer Vision, IEEE (2011) 659–666
10. He, C., Hu, C.H., Zhang, W.: Adaptive shearlet-regularized image deblurring via alternating direction method. In: 2014 IEEE International Conference on Multimedia and Expo (ICME), IEEE (2014) 1–6
11. Hosseini, M.S., Plataniotis, K.N.: Convolutional deblurring for natural imaging. IEEE Transactions on Image Processing **29** (2019) 250–264
12. Bovik, A.C.: Handbook of image and video processing. Academic press (2010)
13. Joshi, N., Szeliski, R., Kriegman, D.J.: Psf estimation using sharp edge prediction. In: 2008 IEEE Conference on Computer Vision and Pattern Recognition, IEEE (2008) 1–8
14. Gokstorp, M.: Computing depth from out-of-focus blur using a local frequency representation. In: Proceedings of 12th International Conference on Pattern Recognition. Volume 1., IEEE (1994) 153–158
15. Oliveira, J.P., Figueiredo, M.A., Bioucas-Dias, J.M.: Parametric blur estimation for blind restoration of natural images: Linear motion and out-of-focus. IEEE Transactions on Image Processing **23** (2013) 466–477
16. Liu, Y.Q., Du, X., Shen, H.L., Chen, S.J.: Estimating generalized gaussian blur kernels for out-of-focus image deblurring. IEEE Transactions on Circuits and Systems for Video Technology (2020)
17. Wen, Y.W., Chan, R.H.: Parameter selection for total-variation-based image restoration using discrepancy principle. IEEE Transactions on Image Processing **21** (2011) 1770–1781
18. Easley, G., Labate, D., Lim, W.Q.: Sparse directional image representations using the discrete shearlet transform. Applied and Computational Harmonic Analysis **25** (2008) 25–46

19. Lim, W.Q.: The discrete shearlet transform: A new directional transform and compactly supported shearlet frames. IEEE Transactions on image processing **19** (2010) 1166–1180
20. Kutyniok, G., Lim, W.Q., Reisenhofer, R.: Shearlab 3d: Faithful digital shearlet transforms based on compactly supported shearlets. ACM Transactions on Mathematical Software (TOMS) **42** (2016) 1–42
21. Xie, S., Rahardja, S.: Alternating direction method for balanced image restoration. IEEE Transactions on image processing **21** (2012) 4557–4567
22. Colton, D., Piana, M., Potthast, R.: A simple method using morozov's discrepancy principle for solving inverse scattering problems. Inverse Problems **13** (1997) 1477
23. Voelz, D.: Computational fourier optics: a matlab tutorial, Society of Photo-Optical Instrumentation Engineers (2011)
24. Zhuo, S., Sim, T.: Defocus map estimation from a single image. Pattern Recognition **44** (2011) 1852–1858
25. Tirer, T., Giryes, R.: Image restoration by iterative denoising and backward projections. IEEE Transactions on Image Processing **28** (2018) 1220–1234
26. Zhang, H., Wu, Y., Zhang, L., Zhang, Z., Li, Y.: Image deblurring using tri-segment intensity prior. Neurocomputing (2020)